High-Responsivity Fiber-Optic Flexural Disk Accelerometers

Geoffrey A. Cranch and Philip J. Nash, *Member, IEEE*

***Abstract*—This paper presents performance measurements of fiber-optic flexural disk accelerometers. The flexural disk acts as a mass-spring element to which the fiber is bonded, such that an acceleration causes a strain to be imposed on the fiber which is measured interferometrically. Simple analytical models have been written to calculate the responsivity and resonant frequency of disks under various boundary conditions and the results of the models have been shown to be in good agreement with the measured responsivity for the case of moderately thick disks. Six optical fiber accelerometers based on flexural disks of different thickness and supports have been demonstrated to exhibit a responsivity in the range from 28 to 39 dB re 1 rad/g with a resonant frequency between 2.4 kHz to greater than 5 kHz, respectively. Of the designs considered, the centrally supported disk is shown to give the highest combination of responsivity and bandwidth. A centrally supported disk has been demonstrated to exhibit a flat response up to 2 kHz and a responsivity of 37 dB re 1 rad/g which when combined with an interferometric phase resolution of 6 μrad/$\sqrt{\text{Hz}}$, would give a minimum detectable acceleration of 84 ng/$\sqrt{\text{Hz}}$. We have attempted to cover all aspects of the sensor design including responsivity, bandwidth, cross-responsivity, phase response and size and find that a complicated compromise between all of these design parameters is required to achieve the optimum performance.**

***Index Terms*—Accelerometers, fiber-optic sensors, interferometric, vector sensor, vibration.**

I. Introduction

DETECTION of sound underwater has, conventionally, been achieved with pressure sensing hydrophones which exhibit an omnidirectional response, where the wavelength of the acoustic signal is significantly greater than the maximum dimension of the hydrophone, as is the case at low acoustic frequency. When such sensors are formed into an array, the outputs can be combined to form beams that can be steered, by applying time delays between the individual sensor signals before recombination. This beam-forming technique allows location of the source of acoustic emission; however, for many array designs there often remains an ambiguity in the precise location of the source due to the symmetry of the array [1]. It generally remains unknown as to whether the source is above or below, or to the left or right of the array. For this reason it is desirable for the sensor to exhibit a directional response over the entire frequency range, which will remove this location ambiguity and hence allow precise location of the source of acoustic emission. A sensor that responds to a vector component associated with the acoustic field, such as the acceleration, velocity or particle displacement, will exhibit this desired directional response and therefore can be used as an alternative to the scalar pressure measurement. The sensor is required to be of low mass and small size compared with the acoustic wavelength, and may be mounted such that it exhibits neutral buoyancy in the array structure.

Development of the fiber optic hydrophone array [2] has led to interest in a fiber optic "vector sensor" that can be interrogated using the same techniques as for the hydrophone array, i.e., interferometry. Fiber-optic-based accelerometers provide all the advantages inherent with fiber optics sensors such as ease of multiplexing, immunity to EMI, an electrically passive sensor and the ability to include in the same network sensors designed to measure different parameters. Recent interest in fiber optic based accelerometers has led to a number of sensor designs being developed [3], optimized for particular combinations of bandwidth and responsivity. The basic design of the accelerometer uses inertial force to generate strain in the fiber, which is measured interferometrically by the effect on the phase of the optical signal propagating through the fiber. The relationship between the induced phase shift and the acceleration is known as the responsivity, $\Delta\phi/\Delta a$, and is expressed in units of radians per g, where 1 g is equal to 9.8 ms^{-2}. The responsivity is often expressed in decibels by calculating $20\,\text{LOG}_{10}(\Delta\phi/\Delta a)$.

One design uses as a sensing element a mass-loaded compliant mandrel, around which the fiber is wound. The sensor demonstrated in [4] achieved a responsivity of 80.4 dB re 1 rad/g and a resonant frequency of 300 Hz with an inertial mass of 542 gramme. A similar type of sensor designed for high temperature applications achieved a responsivity of 52.6 dB re 1 rad/g and a resonant frequency of 413 Hz with an inertial mass of 127.5 g [5]. These sensors, although achieving high responsivity, are less practical for the array applications described above due to their high mass and size, approximately 60 mm in diameter by 70 mm for the device described in [4].

A design, potentially lighter and more compact is based on a flexural disk onto which the fiber is bonded. A design of this type comprising two edge-supported flexural disks demonstrated a responsivity of 34 dB re 1 rad/g and a resonant frequency of 2450 Hz with a mass of 7.7 gramme [6]. A similar design based on a single edge-supported disk achieved a responsivity of 20 dB re 1 rad/g and a resonant frequency of 17 kHz, and in a center-supported disk configuration achieved 19 dB re 1 rad/g and a resonant frequency of 12.5 kHz in a device of size 35 mm diameter by 17 mm [7], [8]. More recently a design consisting of two flexural disks and a large seismic mass

Manuscript received March 1, 2000; revised June 17, 2000. This work was supported by the MOD Corporate Research Programme, TG1.

The authors are with the Defence Evaluation and Research Agency, Winfrith Technology center, Dorchester DT2 8XJ, U.K.

Publisher Item Identifier S 0733-8724(00)08076-2.

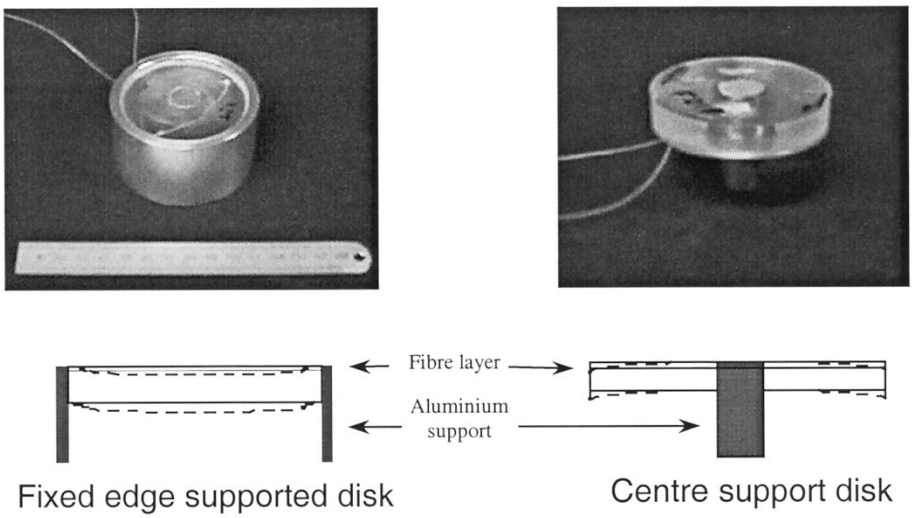

Fig. 1. Principle of operation of the flexural disk sensor.

has demonstrated a responsivity of 69 dB re 1 rad/g and a resonant frequency of 180 Hz [9]. The flexural disk design has, thus, been demonstrated to achieve a range of combinations of responsivity and bandwidth in a device of sufficiently small size and low mass for array applications.

This paper describes work carried out to design flexural disk based accelerometers that are simple to manufacture, exhibit high responsivity and flat frequency response, low responsivity to orthogonal motion, i.e., cross-responsivity, moderately high bandwidth (up to 10 kHz), and small size. The primary aim is to identify the most efficient method of mounting the disk to achieve the highest combination of responsivity and bandwidth. The work carried out has identified this optimum mounting technique in a device of fixed size and fiber length and the sensors that have been constructed exhibit some of the highest combinations of responsivity and bandwidth reported in the literature to date.

A number of disk mountings have been modeled using theory based on small static deflections of moderately thick circular plates and on the dynamic motion of thin circular plates; the models used to predict the responsivity of the disks are described in Section III. The prediction of the resonant frequency of the various disks is then described in Section IV along with an explanation of the treatment of the composite disk structure in Section V. A comparison between the performance achieved by the disks under the various boundary conditions considered is given in Section VI. Sections VII and VIII then discuss the sensor construction and responsivity calibrations. The results and discussion are then given in Section IX. Finally, Section X describes system noise sources.

II. Principle of Operation

The operating principle of the flexural disk sensor is illustrated in Fig. 1. The sensor consists of a coil of fiber encapsulated into the surface of an epoxy disk which is either rigidly supported around the edge or through the center by an aluminum support. An inertial force acting on the support will cause the disk to flex, shown by the dotted line, and this flexing motion induces strain in the fiber coil which is detected interferometrically. The underlying assumption when modeling the sensor is that the central plane in the disk is the neutral surface and any point not lying within this plane will shift its origin, thus inducing a strain. The sensor will exhibit maximum responsivity to the inertial force acting through the axis normal to the disk surface and minimum responsivity when the force acts in the plane of the disk.

III. Modeling the Sensor Responsivity to Acceleration

The responsivity of the flexural disk based sensor can be found by initially calculating the displacements of points in a disk as it flexes under acceleration and converting these displacements into strain in the fiber. The mounting conditions considered are illustrated in Fig. 2(a)-(d) and are referred to as (a) fixed edge support; (b) simple edge support; (c) fixed center support; and (d) simple center support, and these form the boundary conditions. The physical realization of these boundary conditions is discussed later.

The approach used is similar to that described in [10], [11] and extends this analysis for different disk supports and multiple fiber coils. Each model initially calculates the angular displacement, $\theta(r)$, of the disk when exposed to a uniform pressure acting on the top surface as illustrated in Fig. 3 for a center supported disk. This is then used to calculate the strain in a coil at a distance, z, from the neutral surface. By integrating the strain over the surface of the fiber coil and then adding contributions from each coil, if there is more then one coil present, the total strain in the fiber layer is calculated. This is then used to calculate the induced phase change in a light beam travelling through the fiber as a function of the applied pressure. The acceleration responsivity is then calculated by converting this pressure responsivity into an acceleration responsivity.

This calculation is now described in detail for the case of a fixed edge, centrally supported disk. The variables used in the analysis are shown in Table I.

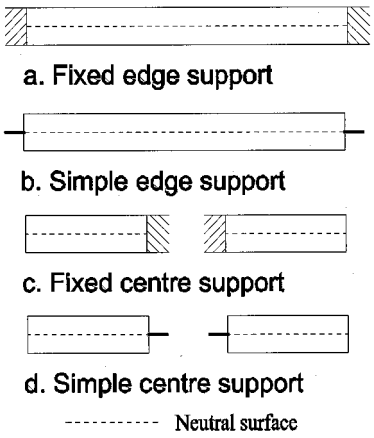

Fig. 2. Mounting configurations for the flexural disks.

The equation for the angular displacement of a fixed edge, centrally supported disk under a uniform force/pressure, ΔP, on its top surface is given by (1) [12].

$$\theta(r) = \frac{M_{rb}}{F_L} r F_5(r) + \frac{Q_b}{F_L} r^2 F_6(r) - \frac{\Delta P}{F_L} r^3 G_{14}(r) \tag{1}$$

where the flexural modulus, F_L, unit shear force, Q_b, unit radial bending moment, M_{rb}, and the general plate functions and constants C_n, F_n, G_n and L_n are given in Table I [13].

Referring to the illustration in Fig. 3, if $\theta(r)$ is the angle subtended by the tangent, at a radial distance r from the disk center, to the horizontal, then the horizontal displacement of a point at a distance z from the neutral surface is given by χ (P to P' in Fig. 3). If the solid line is taken as the neutral surface then a point on the disk, at a distance z along the normal to the neutral surface, will undergo a displacement in the x direction of $\chi = z\theta(r)$ for $\theta \ll 1$, i.e., for small displacements. The strain in a fiber loop of radius, r, and distance, z, from the neutral surface is then calculated from the change in its circumference and is given by (2)

$$\varepsilon(z, r) = \frac{z\theta(r)}{r}. \tag{2}$$

The length of a spiral of fiber of inner radius, b, outer radius, c and a pitch equal to the fiber diameter, D, is given by, $\int_b^c (2\pi r/D)\, dr$. This is then used to calculate the total change in length of a fiber coil subject to a strain, ε, (3).

$$\Delta l(z) = \int_b^c \varepsilon(z, r) \frac{2\pi r}{D}\, dr. \tag{3}$$

If there are multiple coils wound into the disk, they are assumed to be in a hexagonal close-packed structure as shown in Fig. 3. and if there are j coils, the total length change, ΔL, is the sum of the length changes in each coil given by (4).

$$\Delta L = \sum_{i=1}^{j} \Delta l \left(h - (i-1)\frac{\sqrt{3}}{2} D \right) \tag{4}$$

This is obtained by calculating the sum of the change in length of each fiber coil, Δl, which is a function of the distance from the neutral surface, z. Referring to the inset of Fig. 3, the distance of the ith coil from the neutral surface is $h - (i-1)(\sqrt{3}/2)D$. If the fiber coils of total length, L, are incorporated into the arm of a Michelson interferometer, then the phase of the return light at the input is given by (5)

$$\phi = 2nkL. \tag{5}$$

The fractional phase change is then given by differentiation of (5) to obtain (6) and consists of two significant contributions from the axial length change of the fiber and the change in refractive index due to the stress-optic effect (7). A third term that describes the physical change in diameter of the waveguide can be shown to be negligible [14]

$$\frac{\Delta\phi}{\phi} = \left(\frac{\Delta L}{L} + \frac{\Delta n}{n} \right) \tag{6}$$

The second term (the stress-optic effect) in (6) can be shown to be 21% of the first term and of opposite sign, using (7), if the fiber is assumed to be under axial strain only [14] and values of the Pockels coefficent and Poisson ratio of the fiber are taken from Table I

$$\Delta n = -\frac{n^3}{2} (\varepsilon(1 - \nu_f) p_{12} + \nu_f \varepsilon p_{11}) \tag{7}$$

The normalized responsivity to pressure is then given by (8) where the factor of 0.79 accounts for responsivity reduction due to the stress-optic effect

$$\frac{\Delta\phi}{\phi \Delta P} = (0.79) \frac{\Delta L}{\Delta P \cdot L}. \tag{8}$$

Using the relationships that pressure is force per unit area, force is the product of mass and acceleration and mass is the product of volume and density, the normalized acceleration responsivity, $\Delta\phi/\phi\Delta a$, can be calculated from (8). This assumes that the mass is uniformily distributed throughout the disc and is a reasonable assumption to make if the volume of glass in the disc is significantly less than the total volume of the disc. The nonsymetrical distribution of mass will also effect the cross-axis responsivity which is discussed in Section IX. A pressure responsivity is then converted to an acceleration responsivity using

$$\Delta P = 2h\rho\Delta A \tag{9}$$

which gives a normalized acceleration responsivity in units of g^{-1} of

$$\frac{\Delta\phi}{\phi \Delta A} = (9.8) \cdot (0.79) \frac{2h\rho}{\Delta P} \frac{\Delta L}{L} \tag{10}$$

where ρ is the disk density and h is half the disk thickness. It is useful to determine the form of (10) for a simplified case to establish the basic design parameters for the transducer. If the fiber is wound from the disk center, i.e., $b = 0$ to the disk edge $c = a$ then evaluating (1), (3), and (8) for the strain in a single coil wound on the surface of the disk $(z = h)$ gives

$$\Delta l = \frac{2\pi h a^4 \Delta P}{64 D \cdot F_L} \left(\frac{5 + \nu}{1 + \nu} \right) \tag{11}$$

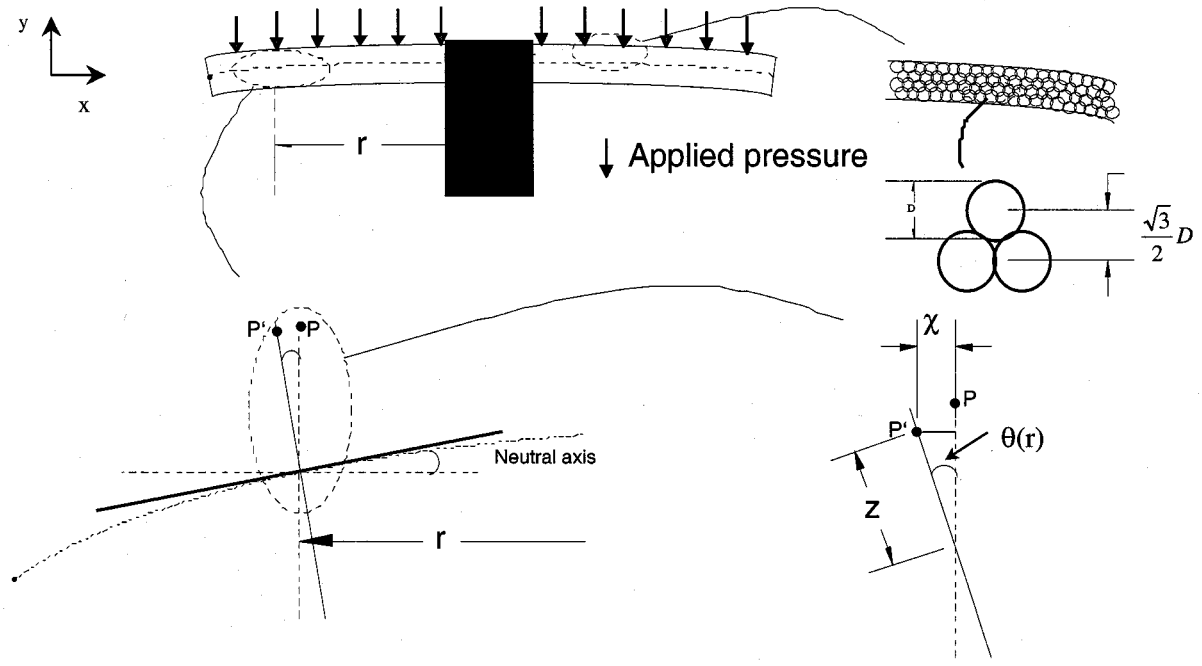

Fig. 3. Illustration of the displacements in a flexing disk.

where ν is the Poisson's ratio of the disk. Thus, from (10) the normalized acceleration responsivity in units of g^{-1} is given by

$$\frac{\Delta\phi}{\phi\Delta A} = (9.8)\cdot(0.79)\frac{3\rho\pi a^4(1-\nu^2)}{32LDhE}\left(\frac{5+\nu}{1+\nu}\right). \quad (12)$$

The acceleration responsivity for a centrally supported disk is therefore proportional to 1) the fourth power of the disk radius, 2) the inverse of the disk thickness, 3) the inverse of the Young's modulus and 4) the disk density. The values predicted by (12) can also be used for validation of the model outputs.

IV. Calculation of the Sensor Bandwidth

The dynamic operation of the flexural disk based accelerometer is modeled by assuming that its motion is analogous to that of a mass-spring system, shown in Fig. 4 [15]. For a simple mass-spring system under sinusoidal oscillation, with a viscous damping coefficient, ζ, and a fundamental resonance frequency of ω_n, the frequency response in terms of the ratio of the relative displacement between the mass and the case, Z, to that of the forcing displacement, Y, is given by

$$\left|\frac{Z}{Y}\right| = \frac{\left(\frac{\omega}{\omega_n}\right)^2}{\sqrt{\left[1-\left(\frac{\omega}{\omega_n}\right)^2\right]^2+\left(2\zeta\frac{\omega}{\omega_n}\right)^2}} \quad (13)$$

and the phase between the two is given by [16]

$$\phi = \tan^{-1}\left[\frac{2\zeta\frac{\omega}{\omega_n}}{1-\left(\frac{\omega}{\omega_n}\right)^2}\right]. \quad (14)$$

It can be shown using (13) that when $\omega \ll \omega_n$, the axial acceleration of the mass will be proportional to the forcing displacement and when $\omega \gg \omega_n$, the displacement of the mass will be proportional to the forcing displacement. In the case of the flexural disk sensor, motion due to the inertia force of interest is transferred to the disk either through the edge or center of the disk causing the disk to flex.

Equations (13) and (14) are plotted in Fig. 5 as a function of normalized frequency, ω/ω_n, with various damping coefficients. For a sensor that exhibits this type of response, the bandwidth is limited, to a first approximation, by the resonance frequency.

It is desirable for the sensor to exhibit a linear phase response with frequency such that transient signals can be detected without significant distortion [17]. Referring to Fig. 5, this is shown by the dashed line plots to occur when the viscous damping coefficient, ζ, is set to zero or 0.7, corresponding to critical damping. When $\zeta = 0$, the phase is zero for $\omega < \omega_n$ and π when $\omega > \omega_n$ and when $\zeta = 0.7$, the phase is proportional to ω for $\omega \ll \omega_n$.

An approximate value for the fundamental resonance frequency of the disk sensor is given by (15) where Λ^2 is the resonance frequency parameter [18] and is tabulated in Table II for the four disk boundary conditions under consideration

$$\omega_n = \frac{\Lambda^2(2\cdot h)}{a^2}\sqrt{\frac{E}{12(1-\nu^2)\rho}} \quad (15)$$

It should be noted that the derivation of (15) neglects rotary inertia and shear forces [21] whose effect become more significant as the disk thickness increases in relation to the drive fre-

TABLE I
DEFINITION OF VARIABLES USED IN MODEL

Symbol	*Typical value*	*Description*
ε		axial strain
a	30 mm	disk radius
b	7.5mm	inner radius of fibre coil
c	28mm	outer radius of fibre coil
E		Average Young's modulus of disk material
ν	0.4	Poisson's ratio of disk material
ρ	1000kg/m^3	Density of disk material
r		radial distance from plate centre
h		half the disk thickness
z		Distance along normal to neutral surface
L		total length of fibre in the sensor
D		fibre diameter
n	1.46	group refractive index of fibre core
λ	1310 nm	Wavelength of light
k	$2\pi/\lambda$	free space wavenumber of light
p_{11}	0.121	Pockels coefficent of fibre
p_{12}	0.270	Pockels coefficent of fibre
ν_f	0.17	Poisson ratio of fibre
j		no. of fibre coils
g	9.8 ms^{-1}	Acceleration due to gravity
P		Pressure
A		Acceleration
F_L	$\frac{E(2h)^3}{12(1-\nu^2)}$	Flexural modulus
Q_b	$\frac{\Delta P(a^2-b^2)}{2b}$	Unit shear force
M_{rb}	$-\frac{\Delta P a^2}{C_8}\left[\frac{C_9}{2ab}(a^2-b^2)-L_{17}\right]$	Unit radial bending moment
C_8	$\frac{1}{2}\left[1+\sigma+(1-\sigma)\left(\frac{b}{a}\right)^2\right]$	Plate constant
C_9	$\frac{b}{a}\left(\frac{1+\sigma}{2}\ln\left(\frac{a}{b}\right)+\frac{1-\sigma}{4}\left[1-\left(\frac{b}{a}\right)^2\right]\right)$	Plate constant
L_{17}	$\frac{1}{4}\left[1-\frac{1-\sigma}{4}\left[1-\left(\frac{b}{a}\right)^4\right]-\left(\frac{b}{a}\right)^2\left[1+(1+\sigma)\ln\left(\frac{a}{b}\right)\right]\right]$	Loading constant
$F_5(r)$	$\frac{1}{2}\left[1-\left(\frac{b}{r}\right)^2\right]$	Plate function
$F_6(r)$	$\frac{b}{4r}\left[\left(\frac{b}{r}\right)^2-1+2\ln\left(\frac{r}{b}\right)\right]$	Plate function
$G_{14}(r)$	$\frac{1}{16}\left[1-\left(\frac{b}{r}\right)^4-4\left(\frac{b}{r}\right)^2\ln\left(\frac{r}{b}\right)\right]$	Plate function

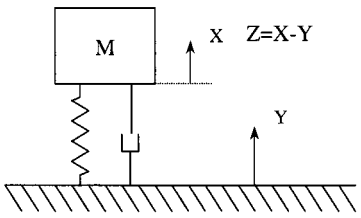

Fig. 4. Simple mass-spring system.

quency [22]. For this reason (15) will predict a higher resonant frequency than that observed for the thick disks.

V. TREATMENT OF THE COMPOSITE DISK STRUCTURE

Calculation of the disk strains is complicated by the presence of the fiber coil, which makes the disk effectively composed of a composite material. The presence of this coil has the following effects; 1) changing the mechanical properties of the disk, i.e., Young's modulus, Poisson ratio and density; 2) changing the position of the neutral surface if fiber is present on only one side of the disk; and 3) affecting the assumption of the pressure-acceleration equivalence as described in Section II. In the models described here, the first issue is resolved by calculating a volume average of the mechanical properties using the rule of

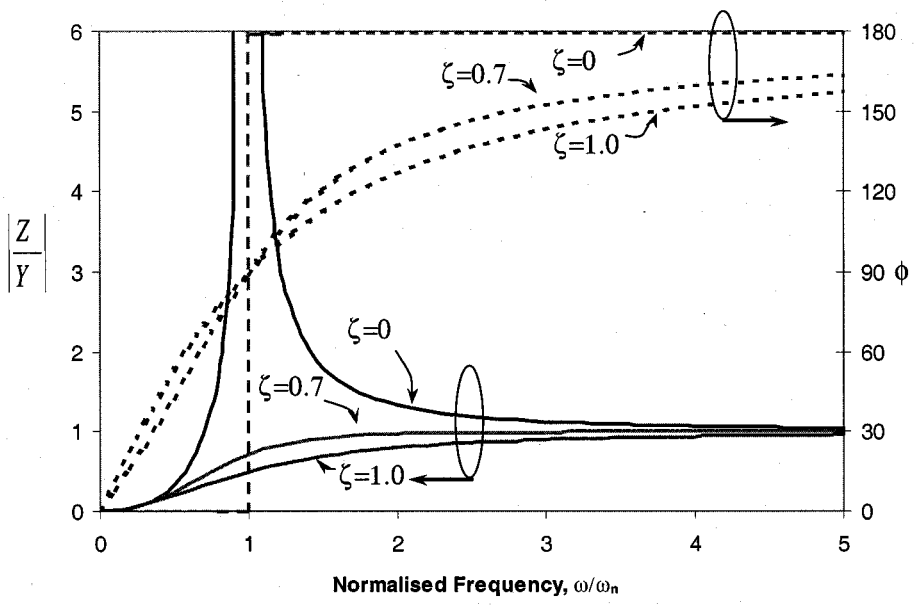

Fig. 5. Mass-spring system frequency response.

mixtures [19]. This has been carried out for the Young's modulus of the disk and adds a correction that becomes more significant as the length of fiber in the coil increases. For example, a disk of diameter 60 mm, thickness 5 mm and consisting of a single coil with 70 m of optical fiber has a volume averaged Young's modulus of 1.6 times that of the encapsulant. This increases to 2.4 times that of the encapsulant with a 2-mm-thick disk and the same length of fiber. The effect on the Poisson's ratio and density is considered to be insignificant. The second issue is taken into account by calculating the position of the neutral surface. As the thickness of the fiber layer increases, the position of the neutral surface will move toward it. Without including this effect, the model described above will overestimate the responsivity of the disk since the coil strain is proportional to the distance from the neutral surface given by (2). The disk can be considered to be a two layer composite, where the top layer exhibits the properties of the fiber/epoxy composite calculated using the rule of mixtures and the bottom layer is epoxy. By using the technique of equivalent sections described in [20], the position of the neutral surface is found by locating the center of area, i.e. centroid, of the equivalent section. This is then added as a correction to the distance of the fiber coil from the neutral surface in (4). For example, if the dimensions of the two layers are as shown in Fig. 6(a) where the top and bottom layers have a Young's modulus of E_1 and E_2, respectively, and $E_1 \gg E_2$, the equivalent section can be drawn assuming it to made from a material of Young's modulus of E_2 as shown in Fig. 6(c).

The actual stress distribution obtained within the disk under bending is shown in Fig. 6(b) and the neutral surface can be located as the point of zero stress. The stress distribution within the equivalent section is also shown in Fig. 6(d) and although this does not represent the actual stress distribution in the disk, it

TABLE II
RESONANCE FREQUENCY PARAMETER

Boundary condition	Λ^2
Fixed edge support	10.216
Fixed centre support	5.76
Simply edge support	4.964
Simply centre support	3.24

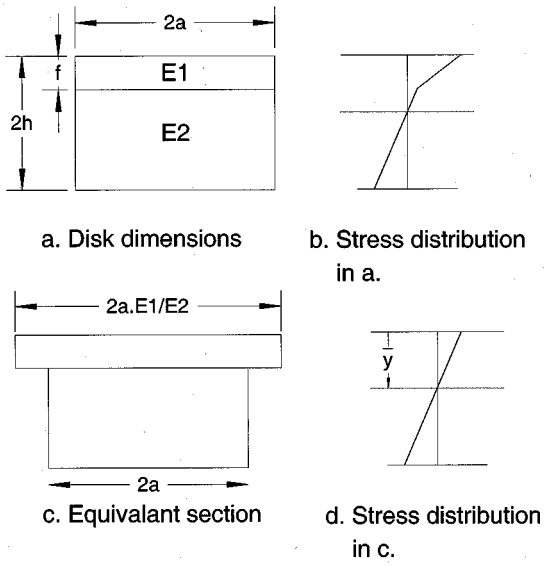

Fig. 6. Equivalent section of composite disk.

can be used to locate the neutral surface. The centroid, $\bar{y}$, is then found by equating the product of the total area of the equivalent section and the distance to its centroid to the sum of the product of the areas of each layer of the disk and the distance to their

TABLE III
COMPARISON BETWEEN EDGE AND CENTRE SUPPORTED DISKS*

	Configuration		
Parameter	*Fixed edge support*	*Simple edge support*	*Fixed centre support*
Disk Thickness, mm	3.0	7.6	6.0
f_{res}, kHz	3.8	3.8	3.8
Responsivity, dB re 1 rad/g	27.4	37.8	35.9

* Here E_{glass}=72 GPa, E_{epoxy}=3 GPa, D=135 μm, a=30mm, b=7.5mm, c=29mm, n=3, fibre length = 54.8m and other parameters are taken from Table I.

centroid (16), where these distances are taken from a common reference point, i.e., the top of the disk

$$\left(2a(2h-f)+\frac{E_1}{E_2}2af\right)\bar{y} = \left(\frac{E_1}{E_2}2af\right)\frac{f}{2}+2a(2h-f)\frac{(2h-f)}{2} \quad (16)$$

The distance to the neutral surface is, therefore

$$\bar{y}=\frac{E_1f^2+E_2(2h-f)^2}{2E_2(2h-f)+2E_1f}. \quad (17)$$

VI. Determination of Important Design Parameters of the Sensor

It is useful to make some preliminary observations on the responsivity and bandwidth that can be achieved with disks under different boundary conditions using the above analysis. A direct comparison will now be made between a fixed center, a fixed edge and a simple edge supported disk configuration using the analysis given in Section III, by determining the highest responsivity obtainable from a disk under each boundary condition for a given resonant frequency. The equations for the strains in fixed edge and simply edge support can be found in [23].

In these calculations, the diameter of the disk and fiber length used are fixed and the disk thickness is varied such that the resonance frequency of each disk configuration is roughly equal. Table III shows this, together with the predicted responsivity of disks in each configuration. The simple edge support exhibits the highest responsivity followed by the fixed center support. The responsivity of the disk in the fixed edge support is significantly lower than the other two since a significant proportion of the fiber is in the region of minimum strain in the disk, i.e., around the edge. In the simple edge and fixed center supported disks, the majority of the fiber is in the region of highest strain. Highest responsivity is therefore obtained when most of the fiber is in the region of largest displacement. Other combinations of the parameters used in Table III arrive at the same conclusions as these.

VII. Sensor Construction

The sensors were constructed by winding a thin coil of optical fiber between two closely-spaced plates and encapsulating the fiber layer in a disk of epoxy resin, type Ciba-Geigy HY1300 and CY 1301. The performance of the sensors is critically dependent on the boundary conditions and it is therefore important to ensure that the disk casing provides the required boundary conditions. For the prototype sensors, the edge-supported disks were bonded inside an aluminum can with adhesive. Centrally supported disks were constructed by encapsulating an aluminum support rod into the epoxy disk. Six sensors were constructed in total with different fiber lengths and disk thickness. Of the six sensors, four were edge-supported and two were center-supported.

VIII. Acceleration Responsivity Calibration

The sensors were calibrated for acceleration using a vibration table, Brüel and Kjær 4809, and a reference B&K accelerometer model 8305 which exhibits a flat frequency response up to 25 kHz. Each optical accelerometer was interrogated using a system configured in a pulsed reflectometric architecture [24] with heterodyne detection. The principle of operation of this system is shown in Fig. 7.

A directional coupler was spliced onto one lead of the sensor coil and mirrors were spliced onto the unused output port of the coupler and the other sensor lead, thus forming a Michelson interferometer. The sensor was then interrogated with two optical pulses, generated by an acoustooptic modulator (AOM) which also applies a frequency difference of 10 MHz ($\Delta f = f_2 - f_1 = 10$ MHz) between them. The optical pulse is generated by driving each AOM by an RF pulse. The separation in time of the two pulses was set to twice the transit time in the interferometer which is achieved by choosing the fiber length in the delay coil within the path balance unit to be equal to twice the fiber length in the interferometer. The return optical signal from the sensor contains an overlap of the two pulses of different frequencies where one has reflected from the first mirror forming the reference and the other has travelled through the sensor. When detected, the overlapping pulses generate a heterodyne carrier signal that is phase modulated when a strain is applied to the sensor fiber. The heterodyne pulse is separated from the rest of the signal with a gate switch, the output of which is bandpass filtered (BPF) and phase demodulated.

In Fig. 7, the optical pulses are shown to be generated by a single AOM; however, in this configuration the interferometer exhibits an effective path imbalance of twice the sensor fiber length. This may cause the phase resolution to be severely degraded by laser frequency noise (discussed later) but can be

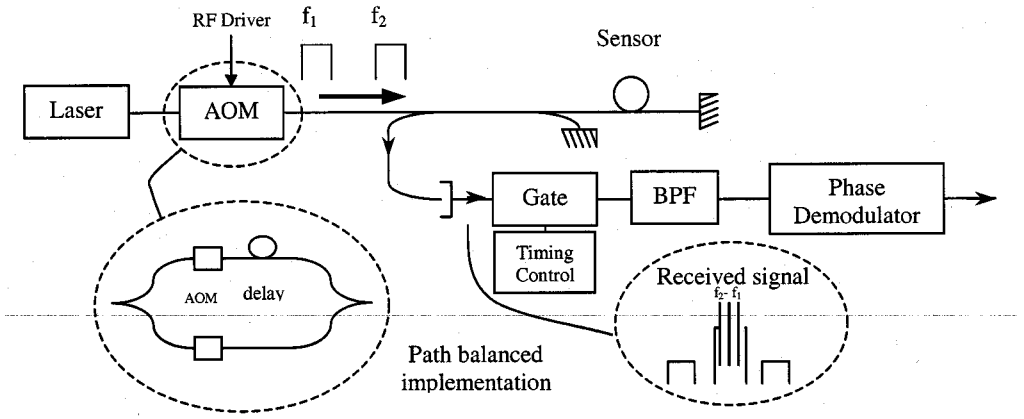

Fig. 7. TDM interferometric interrogation system.

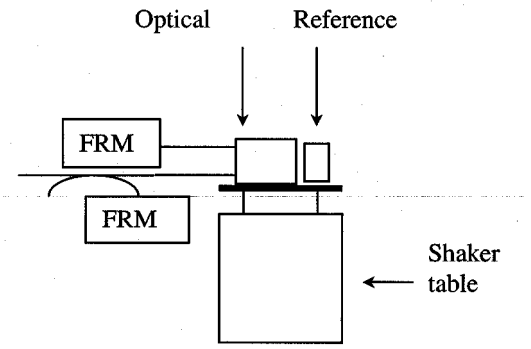

Fig. 8. Experimental setup.

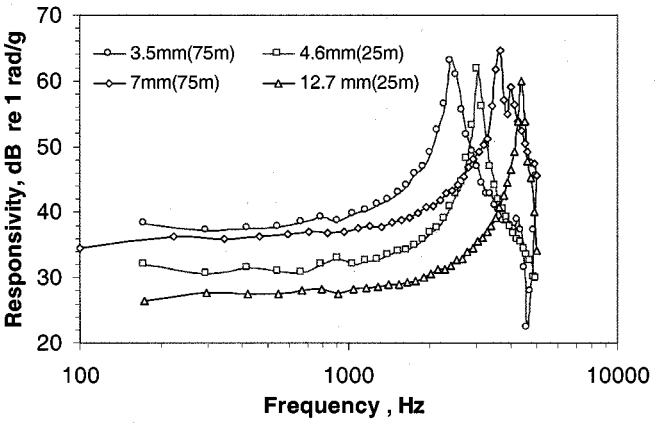

Fig. 9. The responsivity of edge-supported flexural disk sensors for the disk thckness (and fiber length) shown.

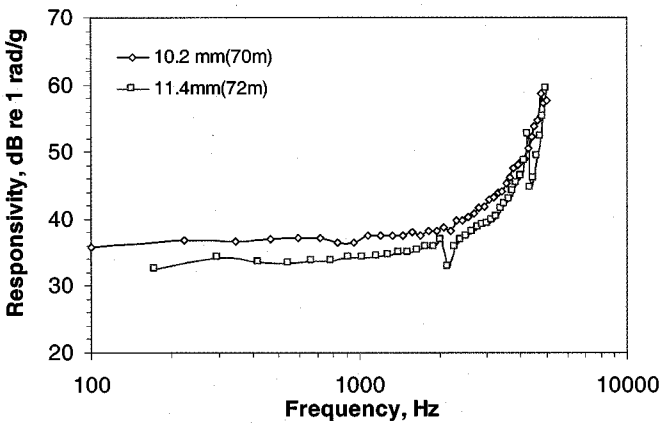

Fig. 10. The responsivity of center-supported flexural disk sensors for the disk thckness (and fiber length) shown.

overcome with a path balanced implementation as shown in the inset in Fig. 7. This generates the two pulses from the same time segment of light and can easily reduce the path imbalance to less than 1 m.

The set-up used to calibrate the sensors is shown in Fig. 8. The optical sensor was placed next to the reference accelerometer on the vibration table. To overcome polarization fading in the interferometer, Faraday Rotation Mirrors (FRM) were used in place of the standard mirrors. This maintains a stable heterodyne carrier despite changes in the birefringence of the sensor fiber [25]. The laser source used was a diode pumped Nd:YAG Lightwave 120 laser.

A frequency response was measured by applying a frequency sweep to the vibration table using a frequency analyzer linked to a PC, to compare the demodulated output of the optical sensor to that of the reference accelerometer. In our measurements the frequency was swept from 100 Hz up to 5 kHz, limited at lower frequency by the phase demodulator low frequency cutoff and at the upper frequency by a resonance of the vibration table. The sensors were placed close together such that they experience the same vibration field.

IX. Results and Discussion

The calibrated acceleration responsivity of the six sensors is plotted in Figs. 9 and 10, corresponding to edge and center supported disks respectively as a function of frequency; the measured responsivities are tabulated in Table IV along with the predicted responsivities and resonant frequencies.

TABLE IV
MEASURED AND CALCULATED RESPONSIVITIES OF OPTICAL ACCELEROMETERS*

			Predicted Responsivity dB re 1 rad/g			*Predicted f_{res} Hz*		
Disk thickness/mm	*Support*	*Measured responsivity*	*Simple*	*Fixed*	*Measured f_{res}*	*Simple*	*Fixed*	*Fibre length /m*
3.5	Edge	39	38.8	26.9	2400	2250	4630	75*
4.6	Edge	32	32.4	24.5	3020	2400	4900	25+
7	Edge	37	38.6	26.9	3780	3930	8100	75*
12.7	Edge	28	28.6	20.1	4380	6200	12750	25+
10.2	Centre	37	44.7	35.4	>5000	3530	5880	70*
11.4	Centre	34	44.3	35.1	>5000	3900	6800	72*

*Here E_{glass}=72 GPa, E_{epoxy}=3 GPa, D^*=135 μm, D^+ +165 μm and other parameters are taken from Table I.

The measured resonant frequency of the disks provides a good indication of the exact boundary condition imposed in practice. Referring to Table IV, the measured resonant frequencies of the edge-supported disk are close to that predicted for a simply supported disk, and the measured responsivity and that predicted for the simply supported disk confirm this. The disparity between the predicted and measured resonant frequency for the thickest edge-supported disk (12.7 mm) is thought to be due to the reasons discussed in Section IV. Hence, the resonant frequency (or bandwidth) cannot be increased without limit by increasing the disk thickness and it is thought that no increase in resonant frequency will be observed with a further increase of the disk thickness.

The resonant frequencies of the center-supported disks cannot be observed directly due to the limited bandwidth of the measurement, however the measured responsivities would indicate that the disks were in a fixed center support. The performance obtained from the center-supported disk demonstrates that a higher overall combination of responsivity and bandwidth can be obtained with this type of disk than that from the edge supported disk.

The responsivity to other directions of acceleration (referred to as the cross-sensitivity) has been measured for the edge-supported disk by rotating the sensor by 90° such that the acceleration acts in a direction parallel to the disk. The calibration described above was then carried out and the result is shown in Fig. 11.

The cross responsivity was found to be typically 8 dB lower than the on-axis responsivity except for the presence of additional apparent resonances at 100 Hz and 1.3 kHz. The exact cause of the 1.3 kHz resonance is unknown but the 100 Hz resonance is thought to be due to the sensitivity of the connecting leads to the sensor and not a mechanical resonance of the sensor itself. Ideally, the sensor should exhibit zero cross-sensitivity, however, in-practice sensitivity to the measurand along this axis may arise for the following reasons 1) The fiber coil may respond to the acoustic signal produced by the vibration table since there is no acoustic isolation; 2) Unwanted resonances of the case may enhance displacements of the disk; 3) For a sensor with a single coil, the nonuniform distribution of the mass causes the center of mass to be shifted toward the coil in the disk. An acceleration force acting parallel to the disk surface will, thus, induce rotational moments, causing the disk to bend; and 4) Deformation of the coil in the plane parallel to the surface of the disk may occur due to the anisotropic nature of the disk stiffness in the fiber layer. Cross-axis sensitivity caused by 1), 2), and 3) can be reduced by appropriate design of the case and by incorporating a second coil on the opposite side of the disk, thus ensuring that the center of mass is located in the central plane of the disk. The effect described in 4) is thought to impose a fundamental limit on the achievable cross-axis sensitivity and needs to be investigated further. A finite element analysis may provide a better insight into this effect.

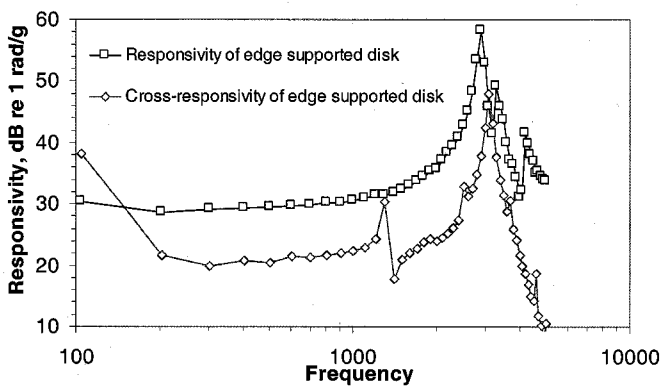

Fig. 11. Edge supported disk responsivity and cross-responsivity.

X. SOURCES OF NOISE IN THE OPTICAL SENSOR AND DYNAMIC RANGE

The primary focus of this work has centerd on maximizing the acceleration responsivity of the sensor, in order to achieve the highest acceleration resolution. The resolution is set by the sensor self noise and in the case of optical fiber sensor systems, the dominant noise sources usually arise from the optical system architecture and components. The fundamental source of noise arises from the shot noise generated on detection of the signal which generates a shot current given by (18)

$$i_{\text{shot}} = \sqrt{2eR\bar{P}} \tag{18}$$

where e is the electron charge, R is the photodiode responsivity and $\bar{P}$ is the average optical power. The received optical power is set high enough such that the shot current dominates over the thermal noise generated in the detector preamplifier. However, in practice it is difficult to achieve the shot noise level due to other sources of noise such as RF oscillator noise (from the acoustooptic modulator drivers) or laser frequency noise which are converted into phase noise by the interferometer. The latter noise source tends to dominate, particularly in multiplexed systems when a significant path imbalance is present in the interferometer. The diode pumped Nd:YAG laser, used in the calibrations exhibits a laser frequency induced phase noise of less than 2 μrad/$\sqrt{}$Hz for frequencies above 100 Hz and a interferometer path imbalance of 1 m [26], however, similar performance can be obtained from a significantly lower cost source based on a single longitudinal mode fiber DFB laser. These have been shown to exhibit a phase noise of less than 4 μrad/$\sqrt{}$Hz for frequencies above 100 Hz and a 1-m fiber path imbalance [27].

In past systems, demodulation of the sensor signal has been carried out with analogue FM demodulators, based on frequency discriminators, that typically achieve a phase resolution of less than 10 μrad/$\sqrt{}$Hz and a dynamic range limited by the maximum frequency deviation that the frequency discriminator can respond linearly to (typically around 90 dB) [28]. However more recently, digital signal processing techniques have been applied to the demodulation process based on sampling of the modulated carrier signal, followed by applying a signal processing algorithm to extract the modulating signal phase. The dynamic range then becomes limited, ultimately, by the sampling rate. A single sensor based system has been developed for DERA by Sensor Dynamics[1] that achieved a phase resolution of 6 μrad/$\sqrt{}$Hz and a dynamic range of greater than 120 dB, where we define the dynamic range as the ratio of the maximum recoverable narrowband signal with less than 1% total harmonic distortion to the noise floor normalized to a 1-Hz bin width [27]. DERA has also recently demonstrated a digital demodulator with the potential to simultaneously demodulate up to thirty channels with comparable performance to that of a single channel digital demodulator [29]. Similar performance using digital demodulation techniques has been demonstrated by other groups [30]. The incorporation of digital techniques provides enhancements in both the electronic phase resolution and dynamic range achievable from such sensors.

XI. Conclusion

In conclusion, six optical fiber accelerometers based on a flexural disk design have been demonstrated that exhibit responsivities in the range from 28 to 39 dB re 1 rad/g with resonant frequencies between 2.4 kHz to greater than 5 kHz, respectively. Simple analytical models have been written to calculate the responsivity and resonant frequency of each disk under various boundary conditions and the results of the model have been shown to be in good agreement with the measured responsivity for moderately thick disks. It has also been shown that the centrally supported disk sensor achieves a higher combination of responsivity and bandwidth than the equivalent edge supported disk. For a centrally supported disk with a flat frequency response up to 2 kHz and a responsivity of 37 dB re 1 rad/g, an interferometric phase resolution of 6 μrad/$\sqrt{}$Hz at 1 kHz would give a minimum detectable acceleration of 84 ng/$\sqrt{}$Hz. This could in principle be reduced by up to a factor of two by attaching a second coil to the opposite side of the disk and operating them in a push-pull configuration. Taking the dynamic range as 120 dB, the maximum narrowband signal recoverable would be about 0.08 g/$\sqrt{}$Hz. The cross-responsivity of the edge-supported disk has also been measured to be at least 8 dB lower than the on-axis responsivity and methods of improving this have been discussed in the text.

Future work will focus on reducing the cross-sensitivity of the sensor and improving the sensor housing.

[1]SensorDynamics Ltd., 3 Abbas Business center, Itchen Abbas, Winchester, Hampshire, SO21 1BQ, U.K.

Acknowledgment

The authors would like to thank Dr. D. J. Hardie and S. Tanner for helpful discussions regarding the development of this sensor and Prof. J. D. C. Jones and Dr. R. McBride for useful comments on the manuscript. Also, we would like to thank S. Way and R. Wilson for help in constructing the sensors.

References

[1] R. J. Urick, *Principles of Underwater Sound*, 3rd ed: McGraw-Hill, 1983, ch. 3.
[2] P. J. Nash, "Review of interferometric optical fiber hydrophone technology," *Inst. Elec. Eng. Proc.—Radar, Sonar Navig.*, vol. 143, no. 3, pp. 204–209, 1996.
[3] D. A. Brown, "Fiber optic accelerometers and seismometers," in *Proc. Acoust. Particle Velocity Sensors: Design, Perform. Applications, AIP Conf.* , vol. 368, Mystic, CT, 1996, pp. 260–273.
[4] D. L. Gardner and S. L. Garrett, "Fiber optic seismic sensor," *SPIE Fiber Optic and Laser Sensors V*, vol. 838, pp. 271–278, 1987.
[5] R. D. Pechstedt and D. A. Jackson, "Performance analysis of a fiber optic accelerometer based on a compliant cylinder design," *Rev. Sci. Instrum.*, vol. 66, no. 1, pp. 207–214, Jan. 1995.
[6] D. A. Brown and S. L. Garrett, "An interferometric fiber optic accelerometer," *SPIE Fiber Optic and Laser Sensor VIII*, vol. 1367, pp. 282–288, 1990.
[7] S. T. Vohra, B. Danver, A. Tveten, and A. Dandridge, "Fiber optic interferometric accelerometers," in *Proc. Acoust. Particle Velocity Sensors: Design, Perform. Applications, AIP Conf.*, vol. 368, Mystic, CT, 1996, pp. 285–293.
[8] S. T. Vohra, B. Danver, A. B. Tveten, and A. Dandridge, "High performance fiber optic accelerometers," in *Proc. 11th Conf. Opt. Fiber Sensors*, 1996, Paper Th5-5, pp. 654–657.
[9] Y. Shindo, N. Tsuchida, K. Dobashi, and H. Kamata, "Fiber-optic accelerometer," in *Proc. 12th Conf. Opt. Fiber Sensors, OSA Tech. Dig.*, vol. 16, Washington, DC, 1997, pp. 202–205.
[10] D. A. Brown, T. Hofler, and S. L. Garrett, "Fiber optic flexural disk microphone," *SPIE Fiber Optic and Laser Sensors VI*, vol. 985, pp. 172–182, 1988.
[11] D. A. Brown, T. Hofler, and S. L. Garrett, "High-sensitivity, fiber-optic, flexural disk hydrophone with reduced acceleration response," *Fiber and Integrated Optics*, vol. 8, pp. 169–191, 1989.
[12] W. C. Young, *Roark's Formulas for Stress and Strain*, 6th ed. New York: McGraw-Hill, 1989. case 2l.
[13] *Roark's Formulas for Stress and Strain*, 6th ed: McGraw-Hill, 1989. case 2l.
[14] C. D. Butter and G. B. Hocker, "Fiber optic strain gauge," *Appl. Opt.*, vol. 17, no. 18, pp. 2867–2869, Sept. 1978.
[15] W. T. Thomson, *Theory of Vibration with Applications*, 4th ed. Cambridge, U.K.: Chapman and Hall, 1993.
[16] *Theory of Vibration with Applications*, 4th ed. Cambridge, U.K.: Chapman and Hall, 1993, pp. 66–67.

[17] *Theory of Vibration with Applications*, 4th ed. Cambridge, U.K.: Chapman and Hall, 1993, pp. 83–84.
[18] "NASA Tech. Doc. SP-160 N70-18461,", 1969.
[19] S. W. Tsai and H. T. Hahm, *Introduction to Composite Materials*. New York: Technomatic , 1980, pp. 388–394.
[20] P. P. Benham and R. J. Crawford, *Mechanics of Engineering Materials*. New York: Longman Scientific and Technical, 1980, pp. 129–132.
[21] "NASA Tech. Doc. SP-160 N70-18461,", 1969.
[22] E. Skudrzyk, *Simple and Complex Vibratory Systems*. University Park, PA: The Pennsylvania State University Press, 1968, ch. 8.
[23] W. C. Young, *Roark's Formulas for Stress and Strain*, 6th ed. New York: McGraw-Hill, 1989. for fixed edge support, case 10b, p. 429, for simple edge support, case 10a, p. 429, for simple center support, case 2k, p. 408.
[24] J. P. Dakin, C. A. Wade, and M. Henning, "Novel optical fiber hydrophone array using a single laser source and detector," *Electron. Lett.*, vol. 20, no. 1, pp. 53–54, 1984.
[25] M. Martinelli, "Time-reversal for the polarization state in optical fiber circuits," in *Proc. 10th Conf. Opt. Fiber Sensors*, 1994, pp. 312–318.
[26] A. D. Kersey, K. J. Williams, and A. Dandridge, "Characterization of a diode laser pumped Nd:YAG ring laser for fiber sensor applications," in *Proc. 9th Conf. Opt. Fiber Sensors*, IROE-CNR, Florence, Italy, 1993, pp. 255–258.
[27] G. A. Cranch and P. J. Nash, "DERA Internal Report,", June 1999.
[28] M. L. Henning and C. Lamb, "At-sea deployment of a multiplexed fiber optic hydrophone array," *Proc. Conf. Opt. Fiber Sensors*, vol. 2, pp. p. 1/84–1/91, 1988.
[29] G. A. Cranch, "DERA Intern. Memo.,", Aug. 1999.
[30] J. Bush, A. cekorich, and C. Kirkendall, "Multi-channel interferometric demodulator," in *Proc. SPIE Third Pacific Northwest Fiber Optic Sensor Workshop*, vol. 3180, May 6, 1997, pp. 19–29.

Geoffrey A. Cranch received the B.Sc. degree in applied physics from the University of Bath, Somerset, U.K., in 1995. He is currently working towards the Ph.D. degree in pysics at Heriot-Watt University in the area of fiber-optic sensors for underwater applications.

In 1995, he joined GEC-Marconi Naval Systems (now Thomson Marconi Sonar) to work on the development of fibre optic hydrophones and in 1997, he moved to the Defence Evaluation and Research Agency, Winfrith, U.K., to continue research on interferometric fiber-optic sensor systems and in fiber Bragg grating sensors.

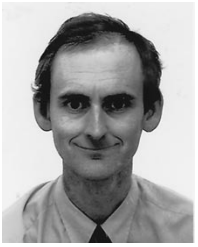

Philip J. Nash (M'99) received the B.Sc. degree in physics from Imperial College, London, U.K., in 1986.

In 1986, he joined Plessey Naval Systems (now Thomson Marconi Sonar), where he worked on the development of fiber-optic hydrophone systems. Since 1994, he has been at the Defence Evaluation and Research Agency, Winfrith, U.K., where he has been managing a number of programmes developing fiber-optic sensors, including hydrophones, accelerometers, temperature and pressure sensors. This work has covered all aspects of sensor development, from sensor modelling through system multiplexing to field trials.

Dr. Nash is a member of the Institute of Physics and a Chartered Physicist.